Article:
Li, Z., Haigh, A.D., Saleh, M.N. et al. (2018) Detection of impact damage in CARBON-FIBRE Composites using an electromagnetic sensor. Research in Nondestructive Evaluation, 29 (3). pp. 123-142. ISSN: 0934-9847

https://doi.org/10.1080/09349847.2016.1263772

DETECTION OF IMPACT DAMAGE IN CARBON FIBRE COMPOSITES USING AN ELECTROMAGNETIC SENSOR

Zhen Li[1], Arthur D. Haigh[2], Mohamed Nasr Saleh[1], Edward D. McCarthy[3,1], Constantinos Soutis[1, 4*], Andrew A.P. Gibson[4] and Robin Sloan[2]

[1]Aerospace Research Institute, The University of Manchester, Manchester, UK

[2]School of Electrical and Electronic Engineering, The University of Manchester, Manchester, UK

[3]Institute of Materials and Processes, University of Edinburgh, Edinburgh, UK

[4]School of Mechanical, Aerospace and Civil Engineering, The University of Manchester, Manchester, UK

Address correspondence to Constantinos Soutis, Aerospace Research Institute, The University of Manchester, Oxford Road, Manchester, M13 9PL, UK.

E-mail: constantinos.soutis@manchester.ac.uk

This paper presents a comprehensive experimental study of impact damage detection for carbon fibre-reinforced polymer (CFRP) composites using an electromagnetic (EM) sensor with coupled spiral inductors (CSI). Two representative types of damage are detected and evaluated, i.e., barely visible impact damage (BVID) and delamination. A multi-frequency inspection is performed, where the resultant images indicate the potential of the CSI sensor in the characterisation of damage extent. The accuracy and efficiency of the CSI sensor are compared with the open-ended waveguide imaging, near-field microwave microscopy, microwave time-domain reflectometry, the complementary split-ring resonator and ultrasonic scanning. Applications and limitations of these non-destructive testing (NDT) methods for identifying impact damage are discussed. There is a free edge effect on the electromagnetic signal, which is illustrated for the first time with the proposed EM technique. Detection of the air gap produced by inserting a thin piece into a machined subsurface groove is carried out. It is found that the developed CSI sensor is able to accurately resolve the location and extent of the air gap. The experimental results demonstrate that the sensor could offer an alternative relatively low cost method that can be fully automated for structural monitoring of aircraft and other composite structures.

Keywords: impact damage, carbon fibre-reinforced polymer (CFRP), non-destructive testing (NDT), electromagnetic sensor, coupled spiral inductors

1. INTRODUCTION

Carbon fibre-reinforced polymer (CFRP) composites are increasingly used in aerospace, marine and automotive industries, due to their superior stiffness and strength characteristics, good fatigue and corrosion resistance and a high strength-to-weight ratio that enables fuel savings [1]. However, the performance of aircraft composite structures can be affected by impact damage, caused by objects and events such as hail stones, runway debris, collision with ground equipment, tool drops and bird strikes. The types of composite damage induced by impact include surface dents, delamination (ply separation or debonding), matrix cracking and fibre breakage. In some low-energy impact cases, damage is hardly visible on the surface, but more severe damage may still exist underneath. Multiple delaminations could develop through the thickness, and the delamination area is significantly increased in comparison to the surface dent [2].

For this reason, different kinds of non-destructive testing (NDT) techniques have been adopted, such as, ultrasonic testing [3, 4], Eddy current technique [5–7], thermography [8], X-ray tomography, optical fibre sensing [9], digital image correlation (DIC) [10], Lamb waves [11] and microwave techniques (e.g., microwave imaging with an open-ended waveguide [12] and near-field microwave microscopy [13]). NDT methods play an important role in the maintenance of structural integrity by enabling timely detection before critical damage occurs. However, at present, no single method exists that can detect all types of defect and damage in all material systems, each method has its own specific advantages and limitations.

Recently, a new kind of electromagnetic (EM) sensor with coupled spiral inductors (CSI) for CFRP composites [14–16] has been proposed. This sensor has several advantages, such as its low power consumption, low cost, potential for high speed

scanning, non-contact, one-sided scanning capability and no need for piezoelectric transducers (e.g., Lamb waves) or couplants (e.g., ultrasonic testing). It operates over a frequency range where the penetration depth is comparable with the sample thickness. The ability to detect an air gap and cracks intentionally produced in a four-layer CFRP plate was reported [14]. Furthermore, the authors optimised the CSI sensor for better impedance matching [17] and extended the applications to the detection of subsurface grooves [18], delamination caused by three-point bending [17] and impact damage [19]. From the detection of subsurface grooves with varied depths and sizes, the pattern of the sensitivity curve was revealed and a linear relationship between the signal response and the location of the defect was established. In addition, an empirical engineering design tool was proposed to relate the setup to its detection performance. In previous work [19], the detection of impact damage using the CSI sensor was limited to either a specific frequency or post-processing of the images produced by the raw data.

In this paper, the potential of the optimised CSI sensor for impact damage detection is thoroughly explored. Firstly, the mechanism and experimental setup are introduced. Two types of damage are discussed, i.e., barely visible impact damage (BVID) and delamination. The detection of the BVID in a plate, an I-shaped beam and samples with varied impact energy levels is carried out. A comparison of the CSI sensor performance with open-ended waveguide imaging, near-field microwave microscopy, microwave time-domain reflectometry (TDR), complementary split-ring resonator (CSRR) and ultrasonic testing is conducted. The effect of the orientation of the sensor on the detection performance and the air gap (one of the characteristics of the delamination) created by a filled subsurface groove are examined, and the effect of the air gap size on the signal response is further analysed.

2. THE EM CSI SENSOR

2.1 Damage Detection Principle

As shown in Fig.1, two square spiral inductors are fabricated on the lower side of a printed circuit board (PCB). By using vias (electrical connections), each inductor is connected to a coplanar transmission line on the upper side to make a two-port sensing device. A sizable defect (e.g., dent, crack or delamination) in the conductive material under test will affect the electromagnetic coupling between the two coils, which can be characterised by the scattering transmission coefficient (S_{21}) [20]. S_{21} is selected rather than other S-parameters because a higher signal-to-noise ratio (SNR) can be achieved. The CSI sensing is similar to Eddy current testing, as both methods are based on the Faraday's principle of electromagnetic induction. However, there are some differences between the two methods, which are listed in Table 1.

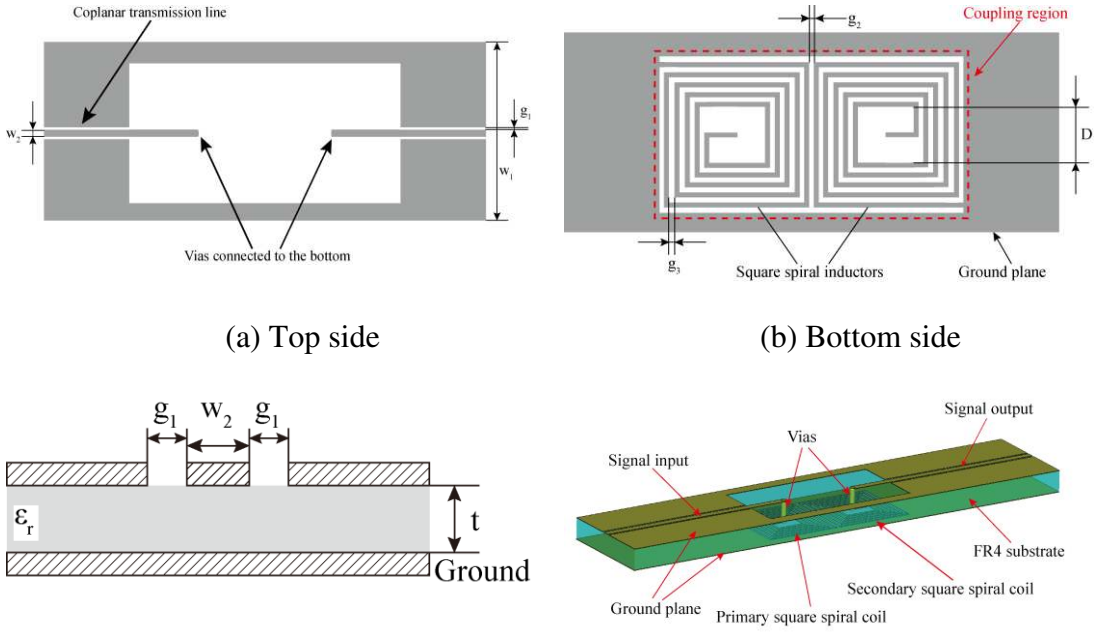

(a) Top side (b) Bottom side

(c) Grounded coplanar transmission line (d) Perspective view

FIGURE 1. Schematic diagram of the CSI sensor

Table 1. Main differences between the CSI sensing and Eddy current testing

	CSI sensing	Eddy current testing
Sensor	Planar coils on a PCB	Three-dimensional coils
Damage indicator	S_{21}	Impedance of the coils
Frequency range	1-500 MHz	Up to 10 MHz
Measuring instrument	Vector network analyser	Impedance analyser
Direction of the magnetic field with respect to the surface	Tangential [14]	Orthogonal

For the original design of the CSI sensor [14], the characteristic impedance of the coplanar transmission line is around 80 Ω, which implies that around 5% energy is reflected during the signal transfer from the SMA connector (normally 50 Ω) to the coplanar waveguide (CPW) transmission line. Here, for the optimised sensor the central track of the CPW line on the upper side shown in Fig.1 (c) is increased to 1.0 mm [17] resulting in reducing the reflected energy to 0.05 %. Detailed parameters of the sensor and corresponding values are presented in Fig.1 (a-c) and Table.2, respectively.

2.2 Experimental Setup

The EM sensor is mounted on an X-Y-Z scanning stage and connected to an HP8753B vector network analyser (VNA) by two coaxial cables for S_{21} measurement. As schematically illustrated in Fig.2, a personal computer (PC) is connected to the PIC18C452 Microchip® microcontroller for the logic control of the stepper motors, which have a high positioning accuracy of 1 µm. A VEE software® programme is applied for the implementation of precise and reproducible movements. In addition, the analyser is connected to the PC by an IEEE-488 cable for data acquisition.

TABLE 2. Dimensions of the optimised electromagnetic sensor

Length of the sensor (mm)	38.40	Inner dimension of each inductor (D, mm)	2.00
Width of the sensor (w_1, mm)	7.80	Number of turns	5
Spacing between the tracks on top (g_1, mm)	0.20	Width of the central track (w_2, mm)	1.00
Spacing between two inductors (g_2, mm)		Thickness of the substrate (t, mm)	1.50
Spacing between each turn (g_3, mm)		Characteristic impedance (Ω)	52.36

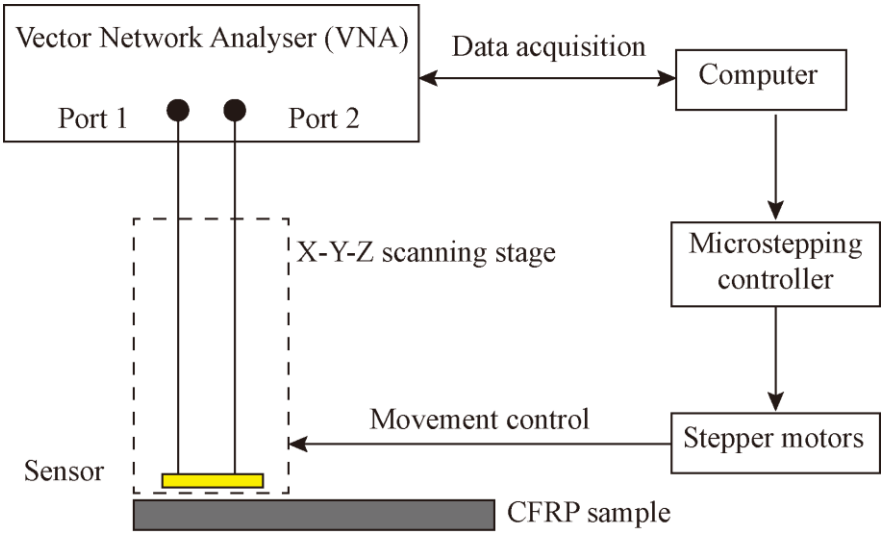

FIGURE 2. Schematic diagram of the experimental setup using the CSI sensor

3. BVID DETECTION

3.1 Impact Damage in a Plate

3.1.1. 2D scanning

In this test, the dent on the top surface of a 4 mm thick CFRP $[+45/90/-45/0]_{4s}$ quasi-isotropic composite laminate was created by a drop-weight impact energy of 20 J. The diameter and depth of the dent observed by an optical microscope were roughly 3.85 mm and 443 µm, respectively. This dent could not be easily found during general visual inspection using typical lighting conditions from a distance of 1.50 m. This kind of damage is categorised as BVID. A non-contact 2D scan was performed with a step size of 403 µm and a standoff distance of 100 µm. The median filtering and mean filtering were applied in the image post-processing for noise reduction and edge enhancement. The magnitude of S_{21} (i.e., $|S_{21}|$) in decibels (dB) is shown in Fig. 3 (a), where the bright area showing higher values (less negative) indicates the location and extent of the dent due to impact at a chosen frequency of 300 MHz. In addition, by subtracting the minimum magnitude value (undamaged position) at each pixel, the magnitude variation $\Delta|S_{21}|$ across the scanned area is presented in Fig.3(b).

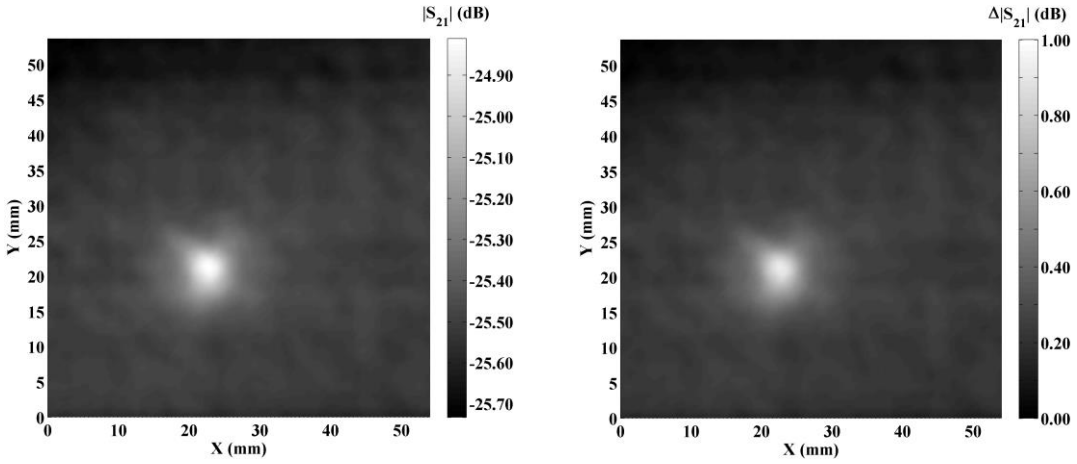

(a) Magnitude plot (b) Magnitude variation

FIGURE 3. The distribution of $|S_{21}|$ at a frequency of 300 MHz

3.1.2. Multi-frequency inspection

Multi-frequency inspection is a common practice when using electromangetic NDT techniques [6], as the penetration of the radio frequency signal is strongly associated with the frequency. Theoretically, for the contact case, the penetration depth d_p in conductive materials can be estimated by [20]:

$$d_p \cong \sqrt{\frac{1}{\pi f \mu \sigma}} \tag{1}$$

where f is the operating frequency. μ is the magnetic permeability of the material, and σ is the electrical conductivity of the sample. In the present case, μ is the permeability of free space μ_0 (i.e., $4\pi\times10^{-7}$ H·m^{-1}), as CFRP is nonmagnetic. The penetration depth will significantly decrease when a higher inspection frequency is adopted. It should be noted that the standoff distance used will affect the penetration depth, as the CSI sensing is a kind of near-field detection technique. The sensitivity to the defects would decrease with increasing standoff distance, and the signal response asymptotes to the free space condition [18].

The effective conductivity of the quasi-isotropic sample was measured using the two-probe method [21]. By substituting the conductivity 2.29 kS/m into Eq. (1), the variation of the penetration depth with respect to the frequency is illustrated in Fig.4, where the horizontal axis is in logarithmic scale for better presentation. The images of $\Delta|S_{21}|$ at four other frequencies are presented in Fig. 5, where the scale of the colour map is the same as that in Fig 3 (b). The apparent size of the impacted region is increased at a lower frequency, which suggests that the internal damage within the penetration depth can be gradually revealed by selecting an appropriate range of frequency (10-500 MHz). Accurate determination of the depth of the delamination can

be done by well-prepared calibration, such as detection of some purposely produced defects with regular shapes [18].

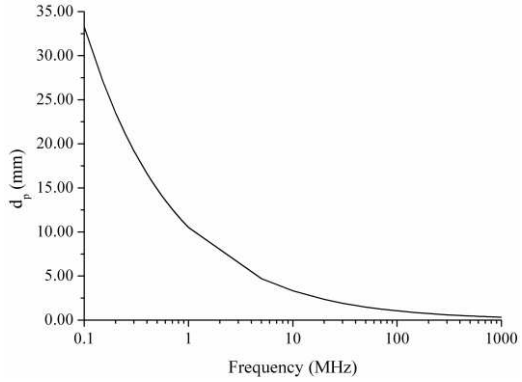

FIGURE 4. Variation of the penetration depth over 0.1 MHz-1 GHz

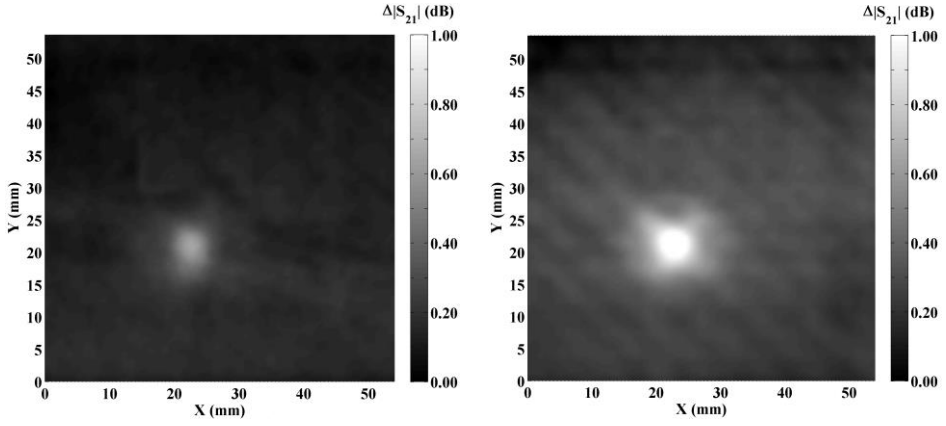

(a) 500 MHz (b) 100 MHz

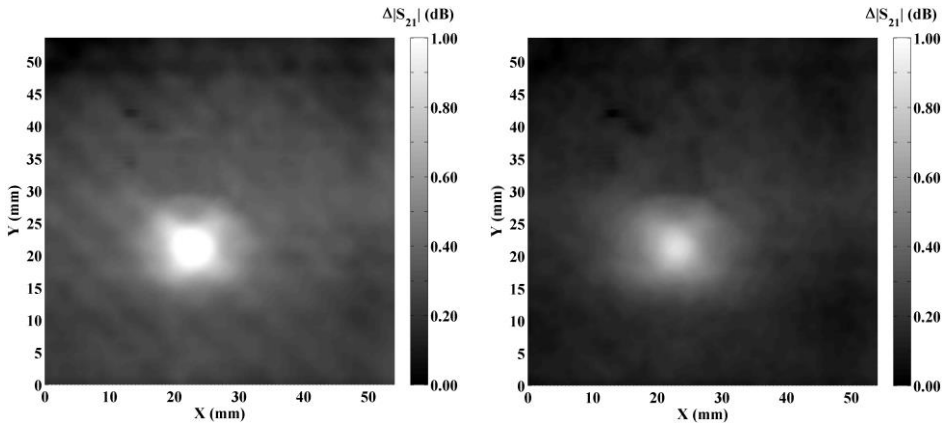

(c) 50 MHz (d) 10 MHz

FIGURE 5. Bright areas indicating the regions of interest at four inspection frequencies

3.1.3. Comparison with other NDT methods

In this section, the sensing performances of the microwave imaging with an open-ended waveguide, near-field microwave microscopy, microwave TDR, a CSRR sensor and ultrasonic testing techniques are compared. The setup and results of each method are described in the following paragraphs:

a) Microwave imaging with an open-ended waveguide: a K -band rectangular waveguide adapter with inner dimensions of 10.70 mm × 4.30 mm was used. A 2D scan was conducted with a step size of 530 μm, a standoff distance of 10 mm and a scanned area of 31.75 mm × 20.64 mm. As a single-port measurement shown in Fig.6 (a), only the reflection coefficient S_{11} at each point was recorded. Fig. 6 (b) illustrates the distribution of the magnitude at 18.5 GHz. The dent can still be identified, while the shape of the dent is slightly oval. The image distortion is mainly due to the intrinsic limited resolution of this technique that is dependent on the waveguide dimensions and standoff distance [22].

b) Near-field microwave microscopy: a near-field microwave profiler developed at the University of Manchester [23] was utilised. As schematically illustrated in Fig. 6(c), the profiler is made up of a microwave closed resonant cavity coupled to a tapered probing tip. When the probe is kept at a fixed standoff distance, defects or a conductivity discontinuity on the surface of the sample can affect the resonance frequency of the cavity. In the test, the resonance frequency at each measurement position was retrieved from a Marconi 6200A scalar network analyser. A 2D scan was performed on the sample with a standoff distance of 100 μm and a step size of 280 μm. The standoff distance was set as small as possible, as only evanescent waves propagate from the tip. In Fig. 6 (d), the area of the dent is clearly defined. In addition, the

symmetric and circular damage shape shows better image quality than the microwave imaging performed with an open-ended waveguide. However, the scanning process of this method is time-consuming. It took approximately 26 minutes to scan an area of 121.64 mm^2 in the present test.

c) Microwave TDR: the methodology of the TDR is based on the fundamental transmission line theory. Any discontinuity in the characteristic impedance along the transmission line caused by the surface defects can be captured from a reflected signal in the time domain [24]. Simpler than the CSI sensor, a CPW transmission line with a length of 90.00 mm was developed [19]. This sensor was placed above the sample with the ground plane uppermost as illustrated in Fig.6 (e). Here, S_{11} (in the frequency domain) was acquired by an HP 3720D vector network analyser. The frequency range 1-18 GHz was utilised with 401 sampling points. Then the data were converted into the time domain by Inverse Fast Fourier Transform (IFFT).

The undamaged and damaged positions were measured with a standoff distance of 100 µm. Signal difference between the two cases in the time domain is given in Fig.6 (f), where the peak of the signal indicates the location of the damage and the horizontal axis is along the length direction. However, the resolution of the image provided is relatively low and unable to reveal the shape and extent of the damage. But it could be improved by optimal design of the sensor configuration; hence, further work is needed especially to optimise the line impedance for a good match in-situ.

d) CSRR sensor: The CSRR sensor commonly used for crack detection in metallic surfaces and permittivity measurement [25] is introduced here. As one of the microwave resonance methods, the resonance frequency of the circuit is the indicator of damage. Similar to the CSI and TDR sensors, PCB fabrication was applied as well. The

geometry of the developed CSRR sensor is given in Fig.6(g), and a microstrip line with a width of 2.8 mm was made on the top of the FR4 substrate. The scan was performed above the sample with a standoff distance of 100 µm. First, the location without impact damage underneath was measured as a reference; then, the region of interest was tested for comparison. The frequency spectrum obtained is illustrated in Fig.6(h). The resonance frequency is increased due to the existence of the damage. A 2D scan can be employed to obtain the location of the damage.

e) Ultrasonic testing: The ultrasonic test was performed with an Olympus OmniScan MX-2®, equipped with a 64-element sensor (transmitter/receiver). The sensor is associated with an encoder that determines its position and enables spatial mapping across the specimen surface [26]. Water was used as the transmission medium in the test. B-scan and C-scan images based on the intensity of the reflected ultrasonic signals are generated. As shown in Fig. 6 (i) and (j), the B-scan reveals the damage distribution through the specimen thickness, while the C-scan is a surface contour plot with all the delaminations stacked together in the top view, which indicates the number and extent of delaminations.

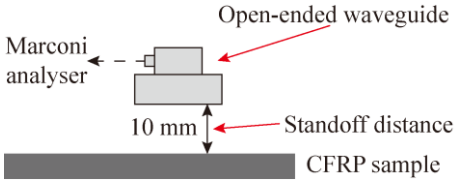

(a) Setup of microwave imaging with an open-ended waveguide

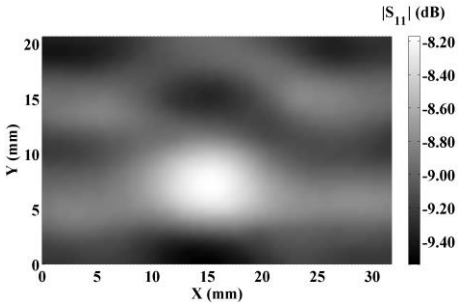

(b) Image by microwave imaging with an open-ended waveguide

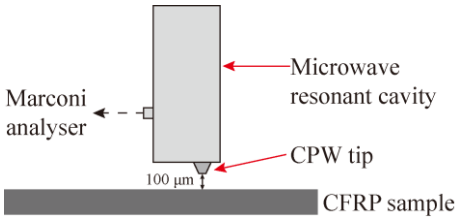

(c) Setup of near-field microwave microscopy

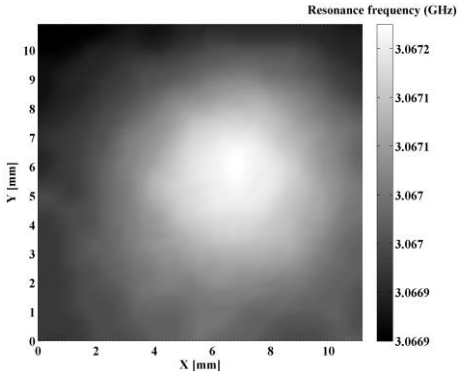

(d) Image by near-field microwave microscopy

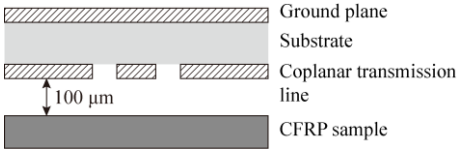

(e) Setup of microwave TDR

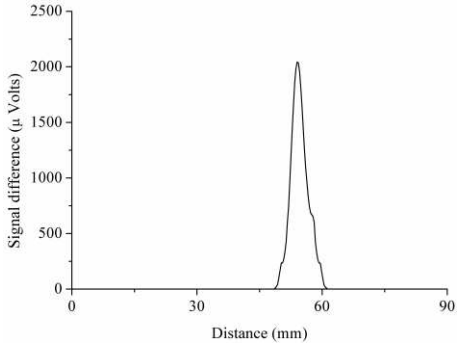

(f) Image by microwave TDR

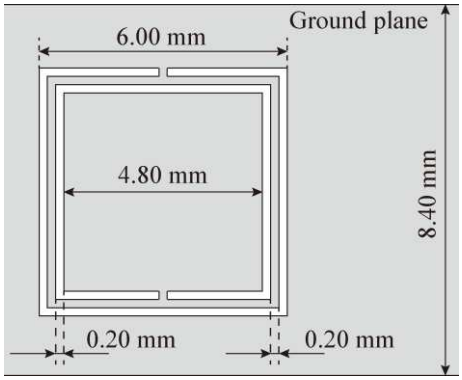

(g) Geometry of the CSRR sensor

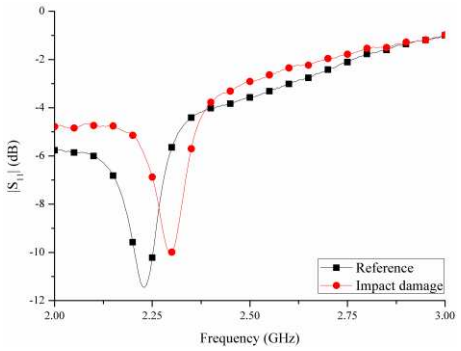

(h) Spectrum of the CSRR sensing

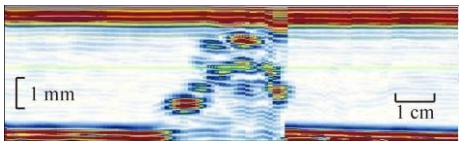

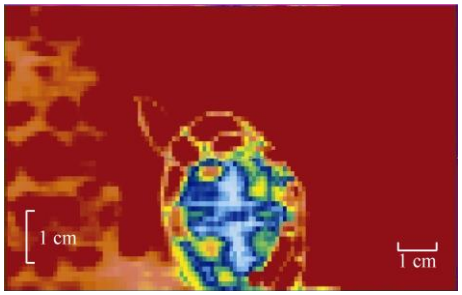

(i) B-scan from ultrasonic testing (j) C-scan from ultrasonic testing

FIGURE 6. Evaluation of the impact damage using five other NDT methods

In summary, among the six NDT methods, ultrasonic testing and CSI sensing could detect both the surface dent and subsurface delamination. However, only the surface defect could be identified by the other four EM NDT methods because of the high frequency range used that limits penetration. In Table.3, inspections using a CSI sensor and the other five above-mentioned NDT methods used for the detection of impact damage in CFRP composites are compared in detail. Some primary factors are listed (e.g., frequency range, cost, equipment setup and scan time) giving an indication of the advantages and limitations to the reader/user.

3.2. Impact Damage in an I-shaped CFRP Composite Beam

3.2.1. Magnitude and phase profiling

An I-shaped composite beam similar to those used in an aircraft structure has been tested. As shown in Fig. 7 (a) and (b), the impact damage was induced on the surface of the top flange, the dimensions of which are 300 mm × 30 mm. The scanning area and the orientation of the sensor for the 2D scanning are presented in Fig. 7(c). The scanning was conducted with a step size of 427 μm and a standoff distance of 250 μm.

TABLE 3. Comparison between CSI and five other NDT methods employed in the test for impact damage detection of carbon fibre composites

NDT methods	**Frequency range**	**Advantages**	**Limitations**
CSI sensor	10-500 MHz	Low-cost (<£10); Reasonable penetration	Point scanning; Accurate positioning needed
Microwave imaging with an open-ended waveguide	18.0-26.5 GHz (K-band)	Easy setup	Limited penetration; Limited resolution
Near-field microwave microscopy	3.0-3.1 GHz	High resolution	Poor penetration; Point scanning; Accurate positioning needed
Microwave TDR	1-18 GHz	Low-cost; Simple fabrication	Relatively complicated data processing; Limited resolution
CSRR sensor	2-3 GHz	Low-cost; Low-power	Point scanning; Limited resolution
Ultrasonic testing	N/A	Good resolution; 3D imaging; Good penetration	In contact; Couplants required

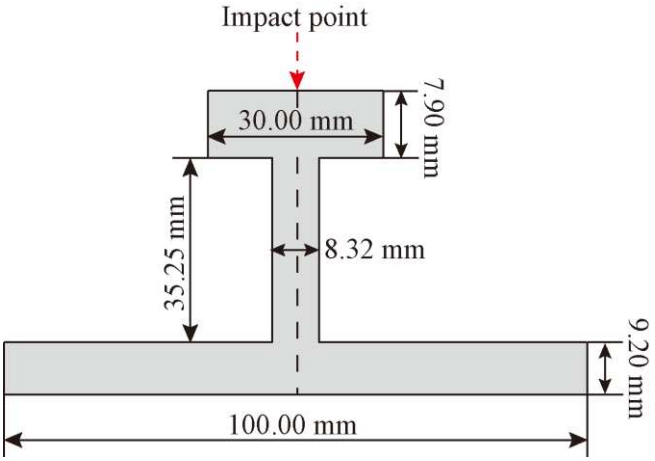

(a) Cross section of the I-shaped beam

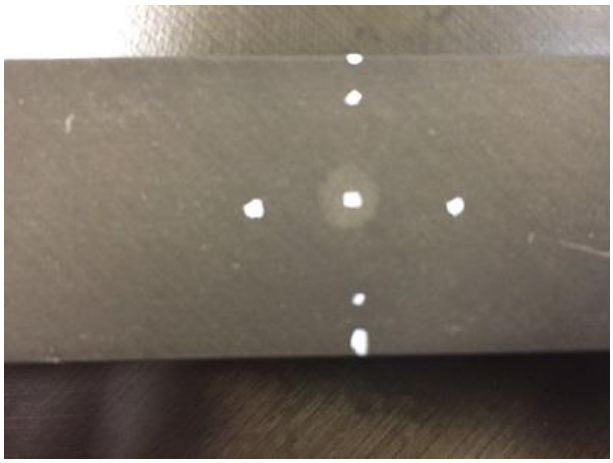

(b) Photograph of the central area of the top flange illustrating the impacted region

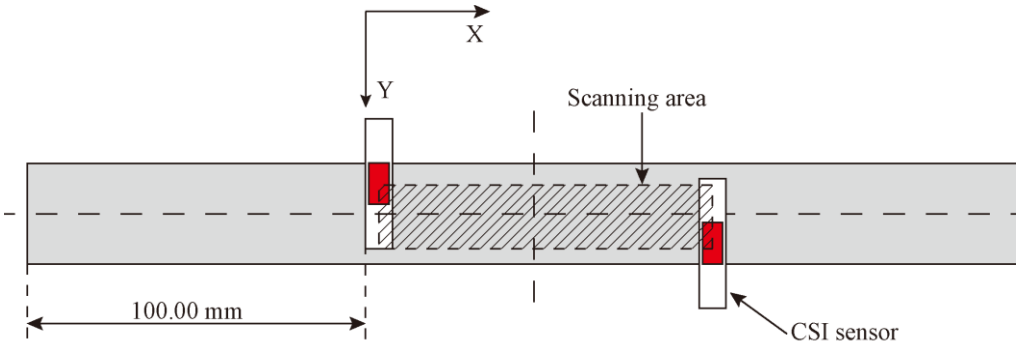

(c) Schematic diagram of the 2D CSI scanning over the top flange

FIGURE 7. Detection of the BVID on an I-shaped carbon-fibre composite beam

Images of S_{21} in the form of magnitude and phase plots are shown in Fig. 8, where the bright region within the red rectangle indicates the impact dent. It is seen that the phase information could be chosen as a damage indicator as well. However, it can be seen in Fig. 8 (a) and Fig.9 that the S_{21} values along the specimen edge are higher than those inside the flange area. This unexpected phenomenon is similar to the edge effect in the Eddy current technique, where the induced currents are distorted near the free edge [27]. Nevertheless, in the present case, the dent-peak in the image is still distinct from edge-peaks for recognition by an experienced operator, as the dent is located a sufficient distance from the edge.

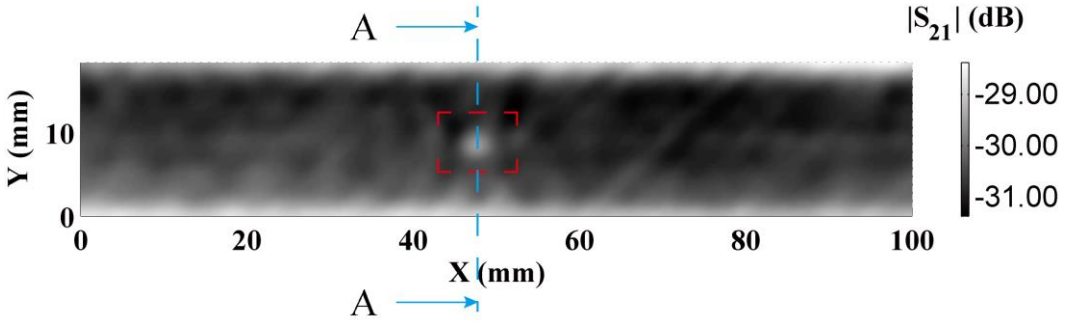

(a) Magnitude

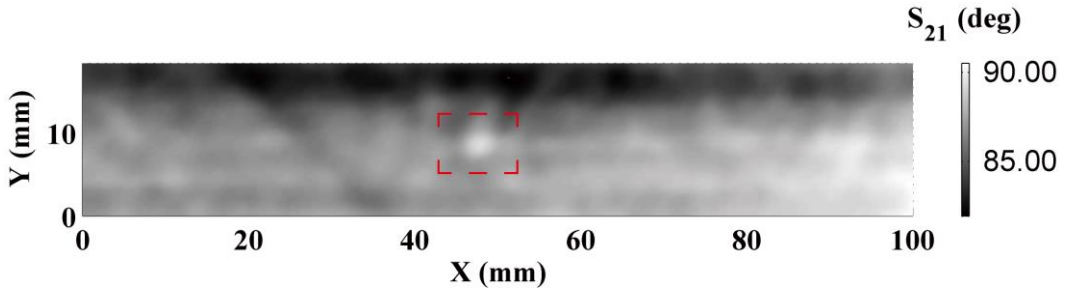

(b) Phase

FIGURE 8. The S_{21} distribution obtained by the impact damage detection of the I beam at the frequency 300 MHz with the sensor perpendicular to X-axis

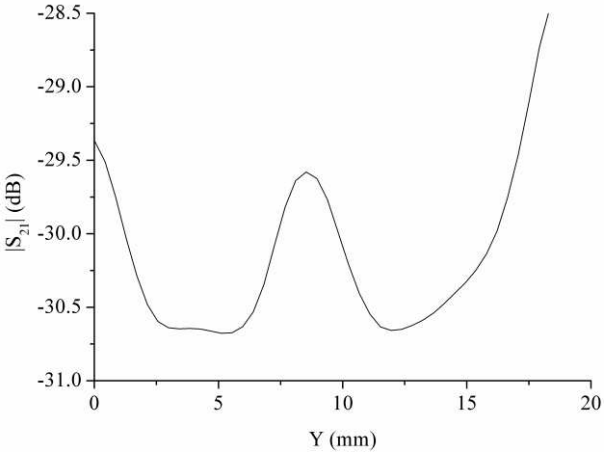

FIGURE 9. $|S_{21}|$ distribution across A-A section (width direction)

3.2.2. Effect of the orientation of the sensor

The effect of the orientation of the sensor with respect to the scanning direction was studied. The vertical orientation along the X-axis was adopted in the tests mentioned above, while the setup of the horizontal case used here is illustrated in Fig. 10. It is observed from Fig. 11 that the BVID is barely identifiable, which is primarily due to the anisotropic characteristics of the conductivity. Hence, the sensor is preferably placed along the fibre direction in order to enhance the sensitivity, as the induced currents flow along the fibres. This of course requires prior knowledge of the curing and stacking sequence of the composite plate for best performance.

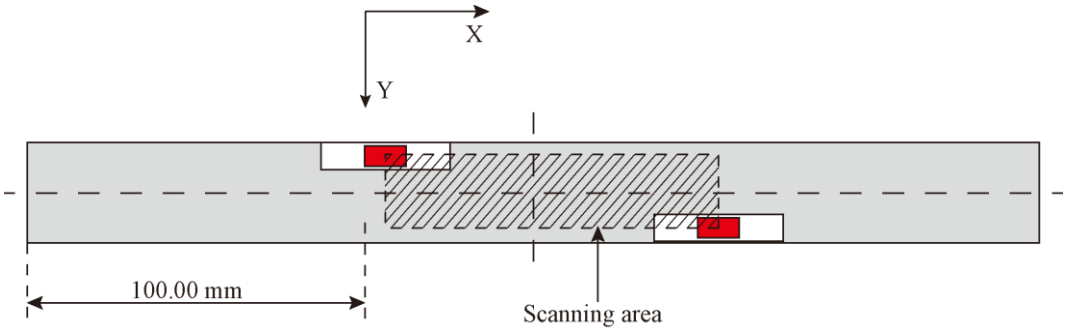

FIGURE 10. Horizontal scan across the surface using the CSI sensor

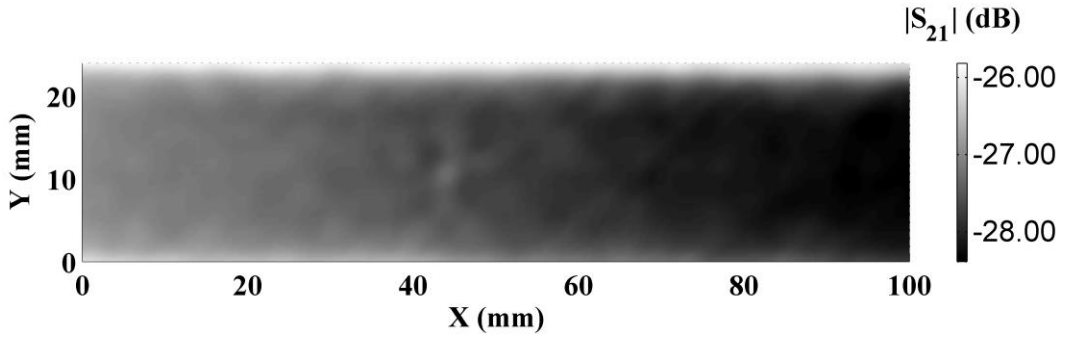

(a) Magnitude

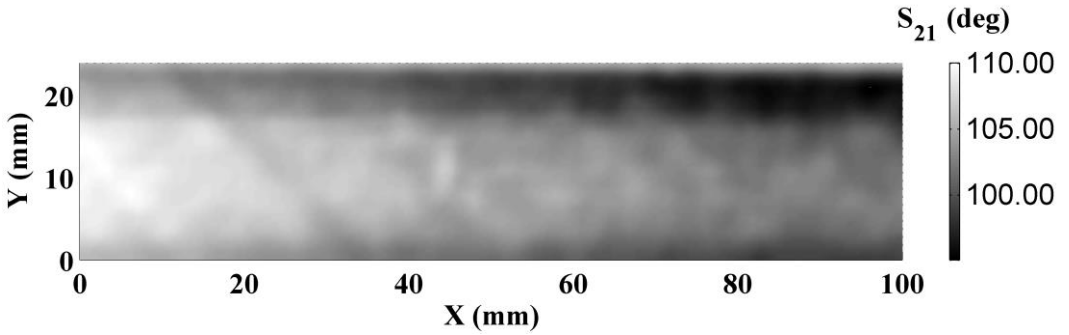

(b) Phase

FIGURE 11. The S_{21} distribution for the case with the CSI sensor parallel to X-axis

3.3 BVID with Different Impact Energy Levels

As shown in Fig.12 (a), four CFRP specimens were impacted at different energy levels, which are 30 J, 45 J, 54 J and 66 J. The location of the impact point for each sample is not the same. A 2D scan was performed with a step size of 403 μm and a standoff distance of 500 μm. As illustrated in Fig. 12(b), the origin of the scan is away from the edge so as to avoid the edge effect. The images of magnitude and phase variations produced at the same inspection frequency of 10 MHz are presented in Fig. 13 and Fig. 14. The dent can be readily observed in all the images. It is found that the size of damage enlarges with the increasing impact energy. The impacted region is better defined at higher energies as would be expected.

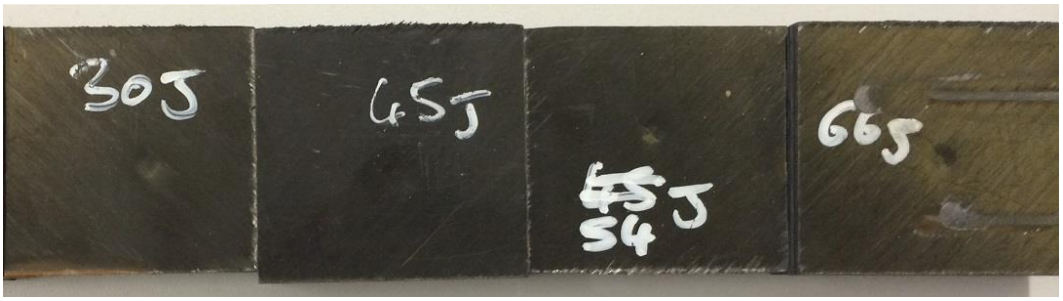

(a) Photograph of four CFRP samples

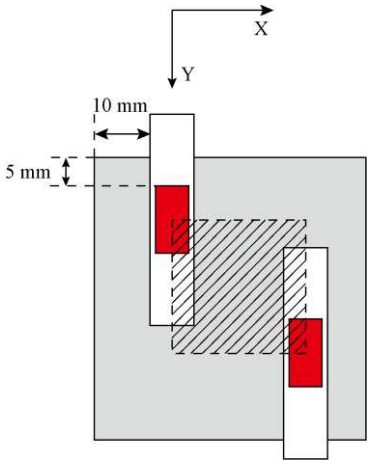

(b) Schematic diagram of the 2D scan

FIGURE 12. Detection of the impacted samples with varied impact energy levels

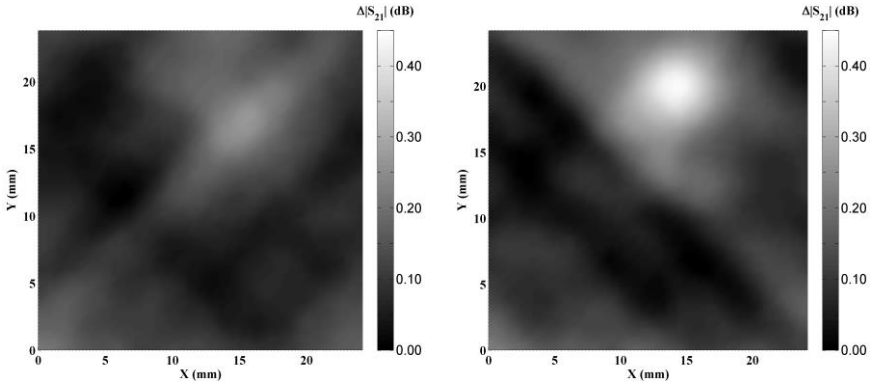

(a) 30 J (b) 45 J

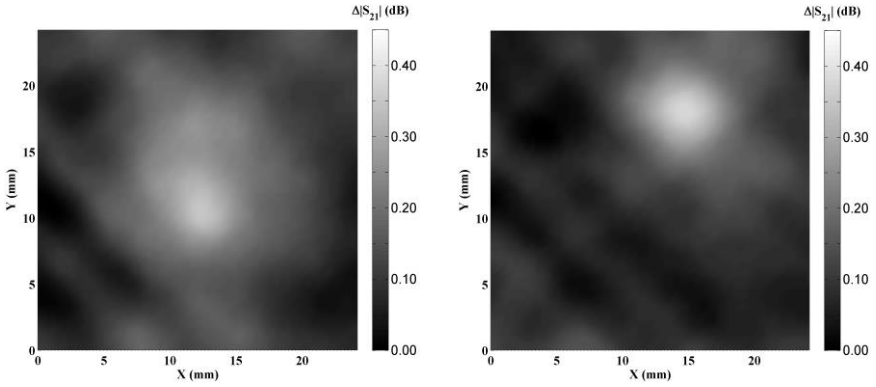

(c) 54 J (d) 66 J

FIGURE 13. Magnitude variations of S_{21} for four different impact energy levels at the same frequency of 10 MHz

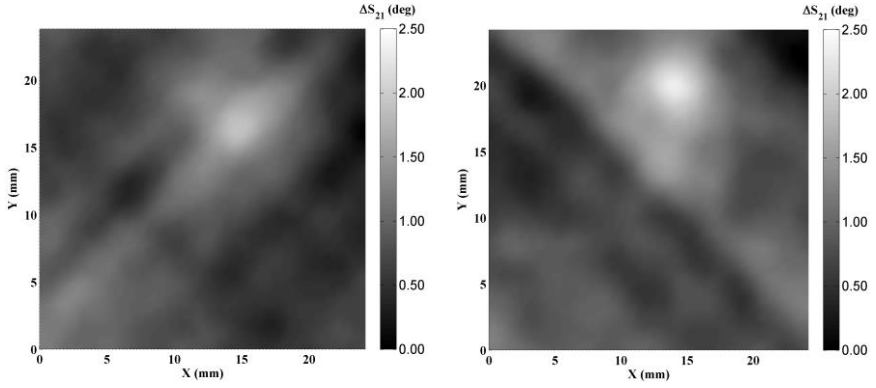

(a) 30 J (b) 45 J

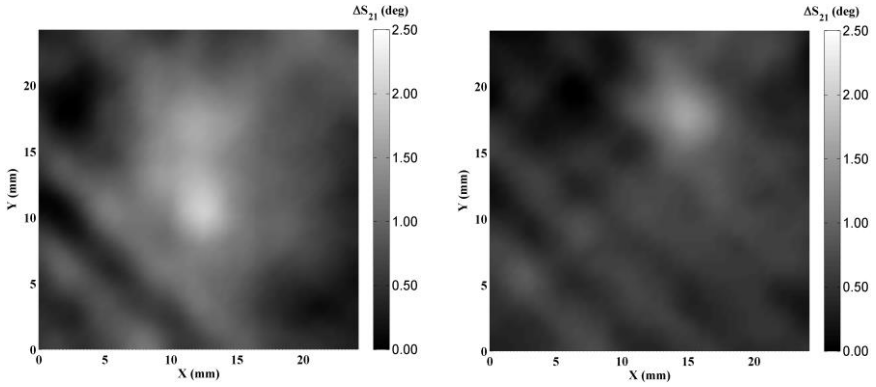

(c) 54 J (d) 66 J

FIGURE 14. Phase variations of S_{21} for four different impact energy levels at the same frequency of 10 MHz

4. DETECTION OF AIR GAPS

The capability of detecting the delamination induced by three-point bending has been reported in previous research [18]. Here, the effect of the air gap size (that could simulate delamination) on the signal response is further studied. In this test, three small fillers with the same width of the subsurface groove (i.e., 4.00 mm) and the same CFRP material were machined as illustrated in Fig. 15, so that an air gap could be produced by partially filling the groove. The thickness of the CFRP panel is 2.58 mm, and the strips are denoted by Strip A, B, C, respectively. The size of each induced air gap is 0.88 mm, 0.54 mm and 0.07 mm, respectively.

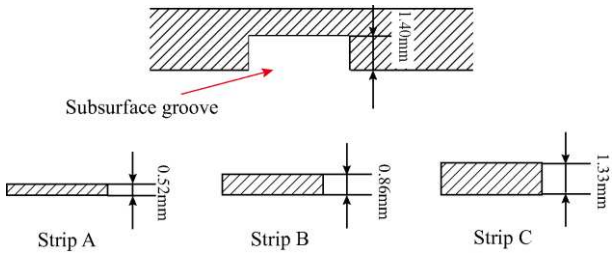

FIGURE 15. Schematic diagram of the subsurface groove and strips for the simulated air gaps

The line scanning was conducted above the defect with a standoff distance of 250 μm and a step size of 127 μm. The effect of the air gap size is evaluated by the signal sensitivity, which is defined as the difference of $|S_{21}|$ (dB) between the origin and the present position. As shown in Fig.16, it is revealed that the sensitivity values is slightly reduced (less than 5%) as the air gap size decreases. This insensitivity to the air gap size could be acceptable in the real world, as real delamination 'thickness' is relatively small compared to specimen thickness.

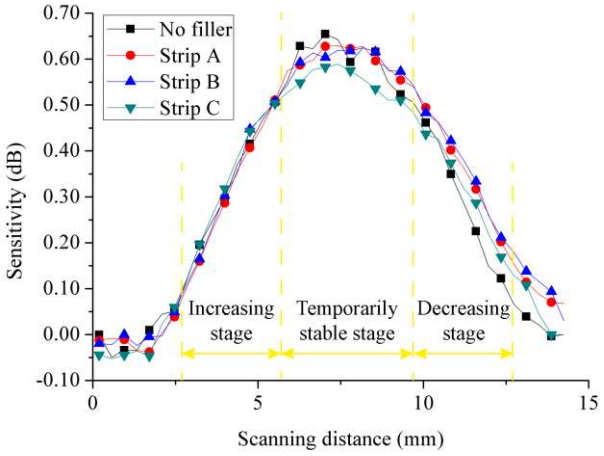

FIGURE 16. Variation of the sensitivity in the detection of the simulated delamination (air gap)

In addition, the trend of the sensitivity curve is in agreement with the three-stage analysis introduced in [18], where the curve experiences increasing stage (Stage I), temporarily stable stage (Stage II) and decreasing stage (Stage III), see Fig.17. The width of the stable stage (approximately 4.00 mm) corresponds to the length of the subsurface groove.

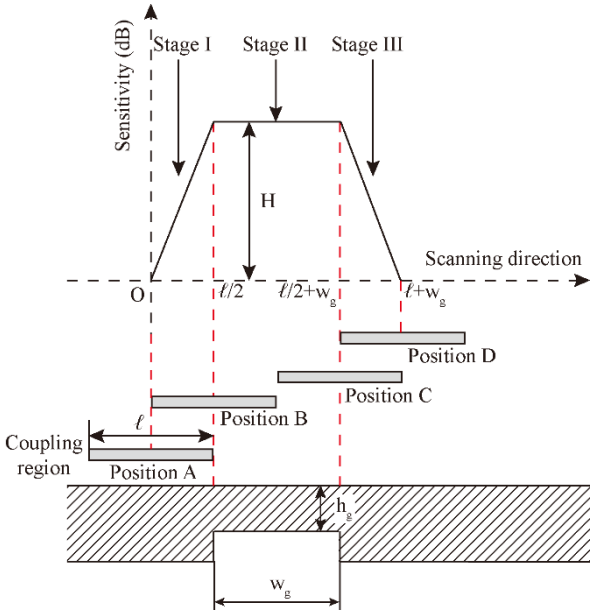

FIGURE 17. Analysis of the interaction between the sensor and the subsurface defect (length of the subsurface groove w_g and the width of the coupling region ℓ) [18]

5. CONCLUDING REMARKS

In this work, the recently developed electromagnetic CSI sensor has been successfully employed for detection and evaluation of BVID and delamination in CFRP composites. The original Salski's CSI sensor is optimised by improved impedance matching. A multi-frequency inspection is performed for the detection of BVID in a composite laminate. The damage propagation through the thickness is characterised by an increase of the region of interest with decreasing inspection frequencies. Five other non-destructive testing methods including microwave imaging with an open-ended waveguide, near-field microwave microscopy, microwave time-domain reflectometry, a complementary split-ring resonator technique and ultrasonic B- and C-scanning have been carried out for comparison. The advantages and limitations of each method for damage detection have been presented for the reader's consideration.

In BVID detection of the I-shaped beam, it has been seen that not only the magnitude data can be used as a damage indicator but also the phase data can contribute to this effort. The edge effect of the CSI sensor is described here to the best of the authors' knowledge for the first time. Current crowding is evident towards the edges of the CFRP and is revealed in this scan. The effect of the orientation on the performance is investigated as well. The optimal orientation of the sensor is dependent on the fibre architecture of the sample under test. The detection of BVID with different impact energy levels has been conducted as well. It is shown that the size of the detected damage increases with the increasing impact energy.

Lastly, the air gap in the CFRP sample created by the combination of subsurface grooves and fillers of various thicknesses (in the effort to simulate delamination) has been examined. It is concluded that the sensor is highly sensitive to the presence of the

air gap. However, further work is required on this since the smallest air gap detected in this work is 0.07 mm, while the gap created by ply debonding in a composite laminate subjected to impact may be smaller, especially if delaminations grow by shear stresses (sliding rather than an opening mode).

ACKNOWLEDGEMENTS

This work was funded by Dean's Doctoral Scholar award, School of Materials, The University of Manchester. Thanks to Kenneth Gyves for his assistance in the laboratory. Special thanks to Dr. Richard Kennon, Dr. Matthieu Gresil and Noushin Karimian for many useful discussions. Thanks also to Professor Prasad Potluri for his guidance and assistance. The authors gratefully acknowledge valuable discussions with Dr. Bartlomiej Salski from Warsaw University of Technology. The authors appreciate the two anonymous reviewers for their valuable comments, which are helpful to improve the paper.

REFERENCES

1. C. Soutis. *Mater. Sci. Eng. A*.**412**:171–176 (2005).
2. Y. Shi, T. Swait, and C. Soutis. *Compos. Struct.* **94**: 2902–2913 (2012).
3. V. Pagliarulo, A. Rocco, A. Langella, A. Riccio, P. Ferraro, V. Antonucci, M. R. Ricciardi, C. Toscano, and V. Lopresto. *Meas. Sci. Technol.* **26**: 085603 (2015).
4. N. Bochud, A. M. Gomez, G. Rus, and A. M. Peinado. *Ultrasonics*.**62**:160-173 (2015).
5. K. Koyama, H. Hoshikawa, and H. Hirano.*Smart materials,structures & NDT in aerospace:*582–594 (2011).
6. W. Yin, P. J. Withers, U. Sharma, and A. J. Peyton. *IEEE Trans. Instrum. Meas.* **58**:738–743 (2009).
7. G. Mook, R. Lange, and O. Koeser. *Compos. Sci. Technol.***61**:865–873 (2001).

8. C. Meola, S. Boccardi, G. M. Carlomagno, N. D. Boffa, E. Monaco, and F. Ricci. *Compos. Struct.***134**:845-853 (2015).
9. D. M. Sánchez, M. Gresil, and C. Soutis. *Compos. Sci. Technol.* **120**:49–57 (2015).
10. M.A. Caminero, M. Lopez-Pedrosa, C. Pinna and C. Soutis. *Compos. Part. B-Eng*.**53**:76-91 (2013).
11. K. Diamanti, J. M. Hodgkinson, and C. Soutis. *Struct. Heal. Monit.***3**:33–41 (2004).
12. S.-H. Yang, K.-B. Kim, H. G. Oh, and J.-S. Kang. *NDT E Int.* **57**:45–51 (2013).
13. L. A. Valiente, A. D. Haigh, A. A. P. Gibson, G. Parkinson, P. J. Withers, and R. Cooper-Holmes.*2006 European Microwave Conference:*718–721 (2006).
14. B. Salski, W. Gwarek, and P. Korpas. *IEEE Trans. Microw. Theory Tech.* **62**:1535–1544 (2014).
15. B. Salski, W. Gwarek, and P. Korpas.*2014 IEEE MTT-S International Microwave Symposium (IMS2014)*:1–4 (2014).
16. B. Salski, W. Gwarek, P. Korpas, S. Reszewicz, A. Y. B. Chong, P. Theodorakeas, I. Hatziioannidis, V. Kappatos, C. Selcuk, T.-H. Gan, M. Koui, M. Iwanowski, and B. Zielinski. *Compos. Struct.***122**:104–122 (2015).
17. Z. Li, A. Haigh, C. Soutis, A. Gibson, R. Sloan, and N. Karimian. *Adv. Compos. Lett.* **24**:44–47 (2015).
18. Z. Li, A. Haigh, C. Soutis, A. Gibson, R. Sloan, and N. Karimian. *Compos. Struct.***140**:252–261 (2016).
19. Z. Li, A. Haigh, C. Soutis, A. Gibson, and R. Sloan. *MIKON 2016 - 21st International Conference on Microwave, Radar and Wireless Communications*, 2016.
20. D. Pozar. *Microwave engineering* 4th ed., p.178. John Wiley & Sons,New York (2011).
21. L. Shen, J. Li, B.M. Liaw, F. Delale and J.H. Chung. *Compos. Sci. Technol*. **67**: 2513–2520 (2007).
22. Z. Li, A. Haigh, C. Soutis, and A. Gibson.*The 53rd Annual Conference of The British Institute of Non-Destructive Testing*, 2014.
23. L. A. Valiente, A. D. Haigh, A. A. P. Gibson, G. Parkinson, G. Jacobs, P. J. Withers, and R. Cooper-Holmes. *2007 European Microwave Conference*:194–197 (2007).

24. A. Todoroki, K. Yamada, Y. Mizutani, Y. Suzuki, and R. Matsuzaki. *Compos. Struct.***130**:174–179 (2015).
25. A. Albishi and O. Ramahi. *Sensors.***14**:19354–19370 (2014).
26. N. Guillaud, C. Froustey, F. Dau, and P. Viot. *Compos. Struct.***121**:172–181 (2014).
27. J. García-Martín, J. Gómez-Gil, and E. Vázquez-Sánchez. *Sensors*. **11**:2525–2565 (2011).